ACS APPLIED ENERGY MATERIALS

www.acsaem.org Article

Direct Patterning of $CsPbBr_3$ Nanocrystals via Electron-Beam Lithography

Christian D. Dieleman, Julia van der Burgt, Neha Thakur, Erik C. Garnett, and Bruno Ehrler*

Cite This: https://doi.org/10.1021/acsaem.1c03091 Read Online

ACCESS | Metrics & More | Article Recommendations | Supporting Information

ABSTRACT: Lead-halide perovskite (LHP) nanocrystals have proven themselves as an interesting material platform due to their easy synthesis and compositional versatility, allowing for a tunable band gap, strong absorption, and high photoluminescence quantum yield (PLQY). This tunability and performance make LHP nanocrystals interesting for optoelectronic applications. Patterning active materials like these is a useful way to expand their tunability and applicability as it may allow more intricate designs that can improve efficiencies or increase functionality. Based on a technique for II−VI quantum dots, here we pattern colloidal LHP nanocrystals using electron-beam lithography (EBL). We create patterns of LHP nanocrystals on the order of 100s of nanometers to several microns and use these patterns to form intricate designs. The patterning mechanism is induced by ligand cross-linking, which binds adjacent nanocrystals together. We find that the luminescent properties are somewhat diminished after exposure, but that the structures are nonetheless still emissive. We believe that this is an interesting step toward patterning LHP nanocrystals at the nanoscale for device fabrication.

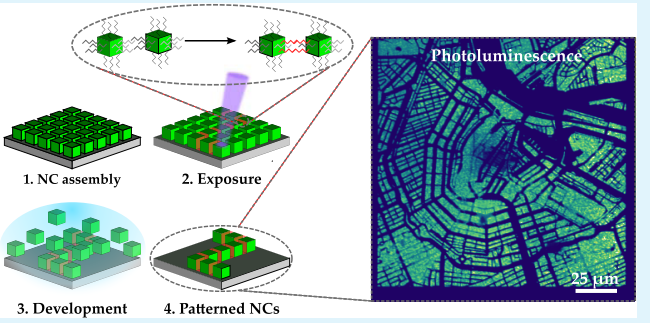

KEYWORDS: *perovskite, nanocrystals, nanopatterning, electron-beam lithography, photoluminescence, AFM, FTIR, nanophotonics*

INTRODUCTION

Perovskite nanocrystals are an interesting material platform for a diverse range of applications. Their simple colloidal synthesis allows for cheap solution processing and the material has an easily tunable band gap. In other semiconductor colloidal nanocrystals, like II−VI quantum dots, the properties like emission and absorption are most commonly tuned by the quantum confinement effect arising from their small size[1,2] and to a lesser extent by their composition, as that requires precise alloying.[3,4] The band gap of perovskite nanocrystals, however, can be readily manipulated via compositional changes, most easily by halide exchange.[5] Mixing of the halides allows for gradual band-gap adjustments.[5,6] Moreover, many different precursors and elements form the perovskite crystal structure, allowing easy substitution of elements and a wide library of possibilities in adapting the material to have desired properties. For instance, by replacing cations, one can form methylammonium-based[7] or formamidinium-based[8] perovskite nanocrystals, and the often-used lead metal can be replaced to form tin-based perovskites.[9] Organic ligands, which passivate the surface of the crystals and provide colloidal stability, can also influence the electronic environment of the nanocrystals and alter the shape during synthesis. This allows perovskite nanocrystals to be suitable for many applications including photovoltaics,[10,11] photodetectors,[12,13] scintillators,[14,15] and light-emitting diodes (LEDs).[16−18] The wide applicability is enabled because perovskites can be efficient emitters, exhibiting long charge-carrier lifetimes and defect resistance. Patterning active materials like these is a useful way to expand their tunability as it may allow more intricate designs that can improve efficiencies or expand the functionality. Patterning materials at the size of the wavelength of light they can emit or absorb can give rise to nanophotonic effects, such as increased absorption,[19] amplified stimulated emission[20] or changes in the wavelength,[21] and the direction of emitted light[19,21] independent from the original material properties. In previous work, we showed a method to pattern colloidal quantum dots (CQDs) directly by extreme UV lithography (EUVL) or e-beam lithography (EBL) without affecting their luminescent properties significantly.[22] In this work, we expanded this method to include perovskite nanocrystals and show that these crystals can also be patterned to create structures down to 100s of nanometers that still show luminescence.

Most of the works on patterning perovskite nanocrystals do not make use of direct lithography. Some approaches include

Received: October 4, 2021
Accepted: January 3, 2022

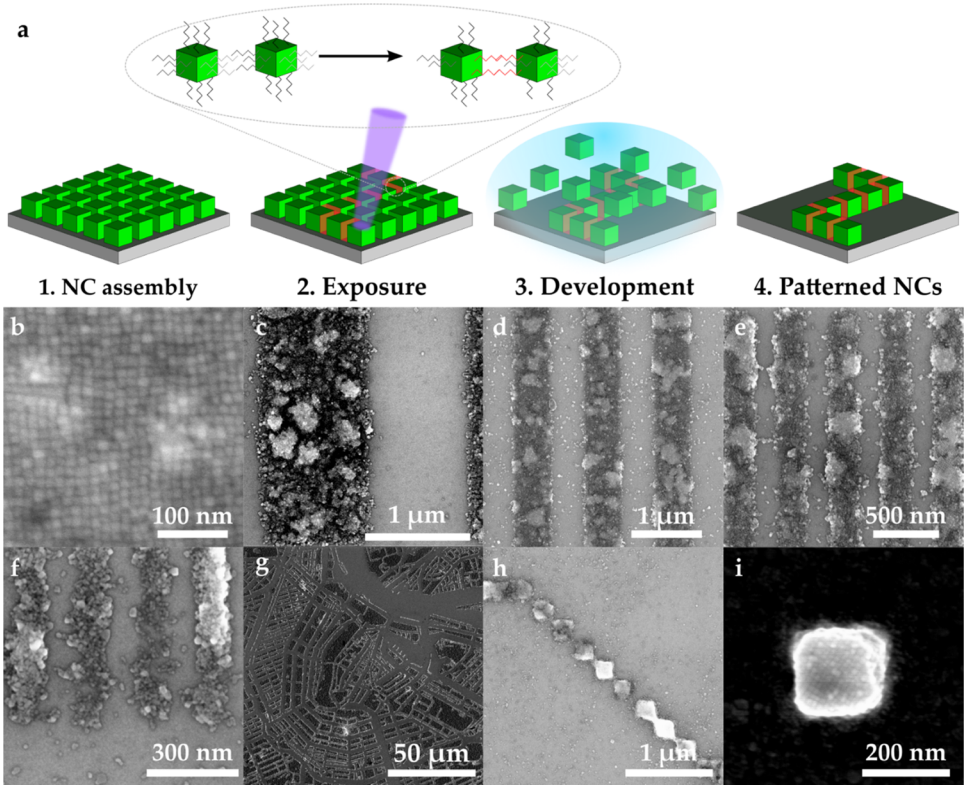

Figure 1. (a) Processing of the patterned nanocrystals. After spin coating (1), the cubic crystals are exposed to a high-energy electron beam (2), which induces cross-linking between ligands of adjacent nanocrystals, as well as some loss of ligands (indicated by the orange layer between the crystals). This makes the new clusters less soluble during the development phase (3), allowing for the selective dissolution of nonexposed nanocrystals and leaving intended structures of nanocrystals behind on the substrate (4). SEM images of unpatterned (b) and e-beam-patterned (c–i) $CsPbBr_3$ nanocrystals at a dose of 2000 $\mu C\ cm^{-2}$. Panel (b) shows the crystals after synthesis, spin-coated into thin films. Panels (c–f) show lines of nanocrystals of 1 μm, 500 nm, 200 nm, and 100 nm widths, respectively. Thinner lines exhibit more apparent line-edge roughness as small variations in particle size have a larger effect on the relative smoothness of the line edge. (g) A pixelated image of the map of Amsterdam consisting of 200 nm × 200 nm pixels. (h, i) Detailed images of these pixels. These structures can be placed with high precision and touch in the corners.

(template-assisted) self-assembly,[20,23,24] laser-assisted deposition,[25,26] ink-jet printing,[27] or multistep lithography.[28,29] Previous work on patterning perovskites via lithography has been carried out by Palazon et al. who showed that the exposure of perovskite nanocrystals to an X-ray photoelectron spectroscopy (XPS) source could impede ion exchange in the crystals and reduce their solubility.[30] They also showed initial patterning with EBL but not with a detailed analysis of its limits and mechanism. It is not obvious that direct patterning with lithographic techniques is straightforward. Although perovskites are often described as "defect-resistant" due to the mobile nature of ions in the crystal, the material also has stability issues, induced by exposure to oxygen, water, or even long exposure to light.[31] In scanning electron microscopy (SEM), it is observed that perovskite crystals can be destroyed under the electron beam.[32] Even though the damage in SEM imaging is induced by the high dose from repetitive scanning across the probe, the highly energetic (but lower-dose) electron beam used in e-beam lithography could also lead to damage of the perovskite nanocrystals, rather than induce local chemical changes that are necessary for direct patterning.

Here, we synthesize $CsPbBr_3$ nanocrystals, spin-coat them into thin films, and expose them directly to an electron beam in a commercial lithography machine. Upon exposure and subsequent development of the films in various solvents, we can create well-defined perovskite structures on the substrate. Feature sizes can be as small as 100s of nanometers. We find that the chemical changes in the ligands induce a cross-linking reaction as well as partial detachment of the ligands that creates a less soluble assembly of nanocrystals. As the required doses are relatively high, we do find some damage to the material in terms of a reduced photoluminescence quantum yield (PLQY). The developed samples are, however, still luminescent, and we believe that this technique is suitable for device fabrication, especially when combined with more efficient cross-linking ligands or repassivation of the crystal surface after processing.

RESULTS AND DISCUSSION

We chose to synthesize and pattern $CsPbBr_3$ nanocrystals as they are known to be relatively stable and have a high PLQY, especially compared to iodide-containing compounds.[8,33] We synthesize $CsPbBr_3$ nanocrystals by adapting the approach of Protesescu[5] and Lu,[34] which comprises the hot injection of a Cs-oleate into a solution of $PbBr_2$, oleylamine (OlAm), and oleic acid (OA) in 1-octadecene. After synthesis and purification, we are left with cubic $CsPbBr_3$ nanocrystals of around 15 nm in toluene. These crystals can be spin-coated onto silicon substrates to form thin layers of nanocrystals with an average thickness of 100 nm. A typical film of nanocrystals can be seen in Figure 1b. The cubic particles arrange themselves into larger-ordered structures. These films are then directly exposed to the electron beam of a commercial EBL machine (Raith Voyager). This machine operates at 50

https://doi.org/10.1021/acsaem.1c03091
ACS Appl. Energy Mater. XXXX, XXX, XXX−XXX

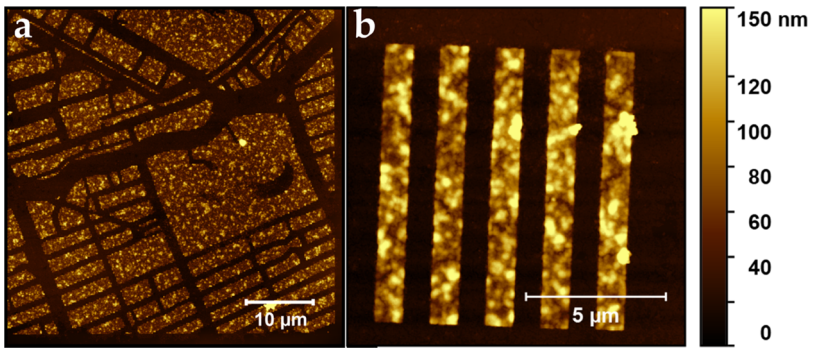

Figure 2. AFM images of patterned $CsPbBr_3$ nanocrystals, with a detail of the map of Amsterdam (a) and the 1 μm lines (b). There is good contrast between the intended structures and the substrate. The thickness is around 100 nm.

keV, and different beam currents can be used for exposing the perovskite films. We expose the films to doses between 100 and 10 000 μC cm^{-2} in line patterns with a width of 50, 100, 200, and 500 nm as well as 1, 2, and 5 μm. After the exposure, we develop the samples in a solvent mixture of chloroform and refrigerated tetrahydrofuran (THF), after which only regions exposed to the electron beam remain on the substrate, resulting in the desired structures formed by perovskite nanocrystals. The schematic of this process can be seen in Figure 1a. Some of these structures can be observed in Figure 1b–h. This behavior, where material becomes partially insoluble upon electron-beam exposure, is reminiscent of negative photoresists that are cross-linked by the electron beam. Unlike commercial photoresists that are typically converted with doses on the order of 100s of μC cm^{-2} due to their high density of functional, cross-linkable groups, the relatively large perovskite nanocrystals need a higher exposure dose of 2000 μC cm^{-2} to obtain a clear structure. This makes the current system less suitable for high-volume manufacturing; however, we have also observed initial results that it is possible to use EUVL in a similar fashion to pattern these materials (Figure S1). With optimization of this method, the process can become viable for high-volume manufacturing in the future. Figure 1c–f shows examples of different line patterns formed by the e-beam patterning. One can observe lines of 1 μm, 500 nm, 200 nm, and 100 nm, respectively. In all cases, the individual nanocrystals can be observed. Down to 500 nm, the lines are very well defined, with remarkably straight edges. When scaling down further, small imperfections start to influence the line-edge roughness to a greater extent. As the nanocrystals we use are cubic, good stacking and self-assembly are beneficial for straight edges. Another factor playing a role in the line-edge roughness is the particle size distribution. Even though in general the nanocrystals are of similar size and shape, larger particles tend to be harder to redissolve during the development process and can lead to less optimal particle assembly. This may disrupt the line edges as is visible in the thinner lines of 200 and 100 nm in Figure 1e,f.

A balance between underexposure and overexposure of the features exists. When underexposing, insufficient material remains on the substrate to form the desired features, while overexposure causes features to blur and leads to more particles remaining on the substrate where not intended. Some examples of this behavior can be found in Figure S2 of the Supporting Information. The optimum doses are relatively high as compared to those of commercial resist materials as well as our previous work with CdSe and PbS quantum dots,[22] on the order of 2000 μC cm^{-2}. This may be related to the larger size of the perovskite crystals used in this work in contrast to the crystal size of previous systems. As the nanocrystal size is growing, the surface-to-volume ratio reduces, and if patterning is dependent on ligand interactions, the reduction of the ratio of ligands to particle volume may be detrimental for the sensitivity. A second reason for the high doses may lie in the binding strength of the ligands to the crystals. Due to the ionic interaction between the ligands and the crystal, ligands on perovskite nanocrystals do not bind as strongly as the ligands in II–VI quantum dots.[35] This may mean that in order for the patterning mechanism to work, more ligands need to cross-link, as otherwise, during development, some cross-linked ligands may simply release from the surface and do not contribute to the cohesion of the crystals.

Figure 1g shows the map of Amsterdam as a pixelated image. Individual pixels are 200 nm × 200 nm, with an overall image size of 150 μm × 150 μm, making this a map with scaling 1: 23 million. In Figure 1h,i, magnifications of the image can be seen in the form of a line of pixels touching at the corners and a single isolated pixel, respectively. These examples clearly show a resolution of 200 nm, and placement of these structures is accurate at the defined positions. In the single pixel, one can also observe the individual nanocrystals. Here, again the influence of the arrangement of the crystals can be observed as the crystals seem to be oriented at a 45° angle with respect to the sides of the square, leading to slightly truncated corners. Although not the focus of this work, it could be interesting to further optimize the stacking of nanocrystals in the future to match the final orientation of the desired features.

Figure 2 shows atomic force microscopy (AFM) images of the patterned nanocrystals. Good contrast of the patterns is achieved between the substrate and thick structures on the order of 100 nm. This thickness corresponds to film thicknesses that are relevant for device fabrication. There appears to be an increased roughness in the film after patterning, most likely due to changes in the ligand arrangement after the cross-linking that can cause the local expansion or contraction of the material, possibly reducing the adhesion between two layers of nanocrystals. The development process can also influence roughness, as during the development phase, some crystal facets that are less well protected by ligands locally dissolve and possibly reprecipitate.

Patterning perovskite nanocrystals does not serve a function if their intrinsic functionality is lost. The photoluminescence (PL) should therefore remain after processing. We spatially

https://doi.org/10.1021/acsaem.1c03091
ACS Appl. Energy Mater. XXXX, XXX, XXX–XXX

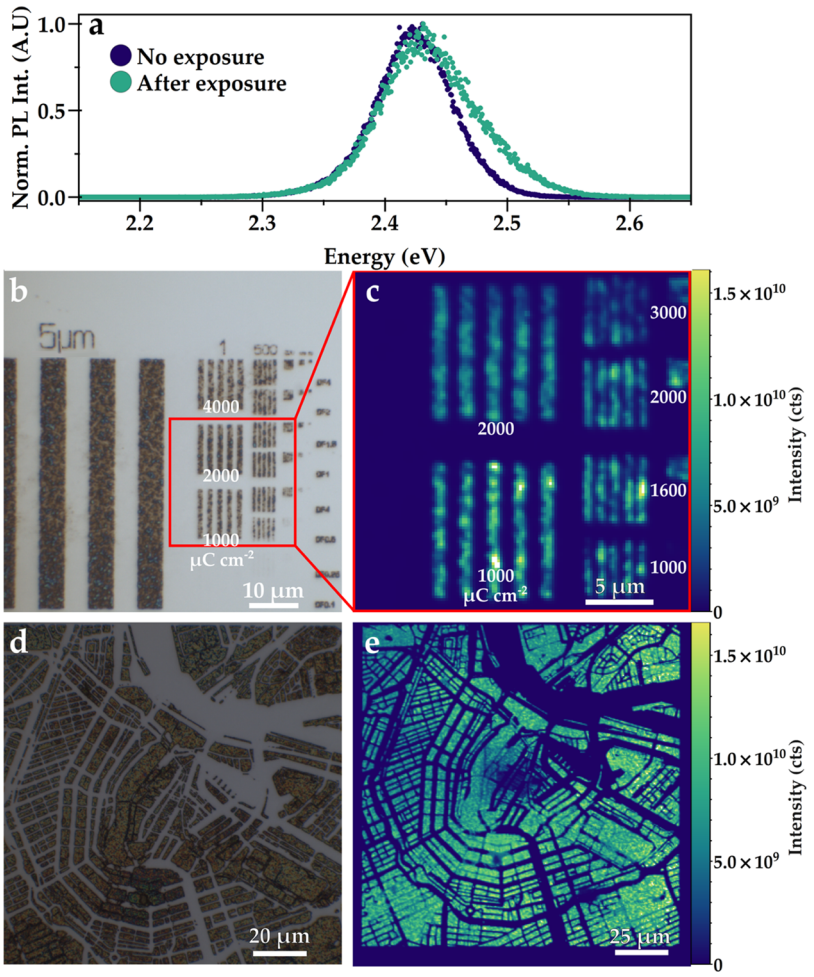

Figure 3. (a) Observed spectrum of patterned and unpatterned $CsPbBr_3$ nanocrystals. The spectra are very similar in shape and have a peak emission at 2.42 eV/513 nm. Optical microscope (b, d) and integrated PL intensity maps (c, e) of patterned $CsPbBr_3$ nanocrystals. Structures are excited with a 405 nm laser, and PL around the peak emission of the perovskite is integrated. Lines with a width down to 500 nm can be spatially resolved with the optical microscope. An e-beam exposure dose of at least 1000 μC cm^{-2} is needed for good contrast. Doses over 2000 μC cm^{-2} diminish the PL intensity. Exposure doses are shown in the images (b, c). The Amsterdam map is exposed at 2000 μC cm^{-2}.

map the PL with a confocal microscope system (WITec alpha300 SR), where the structures are excited with a 405 nm laser coupled into the objective. Figure 3a shows the normalized PL spectrum of the $CsPbBr_3$ nanocrystals before and after exposure (raw data in Figure S3). We observe the typical emission profile of $CsPbBr_3$ with peak emission around 2.42 eV or 513 nm, as observed by others.[5,34] We see a small broadening at the high-energy side after exposure and an increase in full width at half maximum (FWHM) from 0.070 to 0.085 eV. A general broadening of the PL is expected from the exposure as damaging of the material may create more states from where emission is possible. Figure 3 shows optical microscope and integrated PL intensity maps side-by-side for line patterns (b, c) and the Amsterdam map (d, e). The exposed and developed structures are still very brightly luminescent and show the same emission line shape as before exposure. The line patterns visible in the PL map have a width of 1 μm in the left column, 500 nm in the middle column, and 200 nm in the rightmost column. Down to 500 nm, lines can be resolved by the microscope due to the high NA of the objective (0.9). The 200 nm lines cannot be spatially resolved, even though emission is detectable from this block of lines. The exposure doses used for patterning in Figure 3 are 2000 and 1000 μC cm^{-2} for the 1 μm lines and 3000, 2000, 1600, and 1000 μC cm^{-2} for the 500 nm lines from top to bottom, as shown in the figure. All lines in this region are similarly resolved after patterning, but PL intensity is slightly less bright for higher doses. For the 200 nm lines, which are written with the same exposure doses as the 500 nm lines, the story is slightly different. In this case, the lower dose of 1000 μC cm^{-2} is not enough to form a thick structure and thus PL is not very bright. At least 1600 μC cm^{-2} is necessary to resolve a clear structure, but both contrast and PL are higher at 2000 μC cm^{-2}. At higher doses, the PL decreases again. This raises the question to what extent the patterning and exposure dose affects the PLQY, as the dose should be high enough to resolve the structures but low enough to avoid damage to the semiconductor properties.

To estimate the changes in PLQY, we expose a film of $CsPbBr_3$ nanocrystals to different e-beam doses without development and spatially map the absorbance as well as PL. Measuring absorbance requires a transparent substrate. As glass or quartz is not conductive, however, patterning a perovskite layer on top of glass is not possible. The exposure would cause charging of the sample and drifting of the electron beam, which makes proper patterning impossible. Therefore,

https://doi.org/10.1021/acsaem.1c03091
ACS Appl. Energy Mater. XXXX, XXX, XXX−XXX

indium tin oxide (ITO)-coated glass substrates were used to allow for dissipation of charges under exposure. We expose the sample to different doses ranging from 200 to 10 000 μC cm^{-2} (corresponding to dose factor 0.1−5.0). Subsequently, the absorbance and reflectance at 405 nm, the same wavelength used for excitation for the PL measurement, of the exposed area were mapped in an integrating sphere setup described in earlier work.[36] This setup allows us to record the absorption and reflection at the same time. Inspection under the optical microscope already shows that exposure leads to changes in absorbance, as areas exposed to higher doses appear darker (see Figure S4). Figure 4a shows an absorbance map of

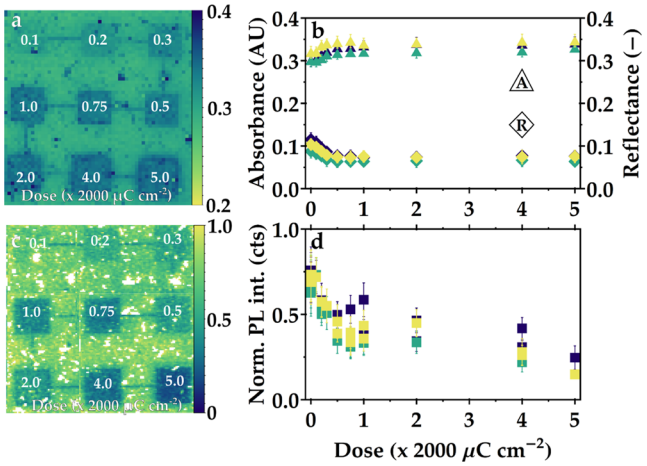

Figure 4. Absorbance, reflectance, and integrated PL intensity of exposed but undeveloped $CsPbBr_3$ films. (a) Absorbance map of the exposed nanocrystal film. White labels indicate the dose factor, which should be multiplied by 2000 μC cm^{-2}. Individual exposure fields are 50 μm × 50 μm. (b) Absorbance (triangles) and reflectance (diamonds) as a function of the exposure dose of three different samples. (c) PL intensity map with the relative PL intensity per exposure dose. (d) Average PL intensity as a function of exposure dose for three different samples.

exposure fields on an undeveloped $CsPbBr_3$ film. Figure 4b shows the measured absorbance (triangles) and reflectance (diamonds) as a function of exposure dose. The error bars indicate the standard deviation of the measured absorbance over the pixels of each dose in the exposure field. We show the results of three samples, which show a similar trend, although absolute absorbance and reflectance values may change from sample to sample. The full absorbance and reflection maps can be found in Figure S5 in the Supporting Information (SI). We observe an increase of the absorbance from 0.30 ± 0.02 of the unexposed film to about 0.34 ± 0.01 at 2000 μC cm^{-2}, after which the absorption only increases very slightly even when the exposure dose is 5 times higher. This increase in absorption may be an explanation for the observed broadening of the PL on the high-energy side of the spectrum (Figure 3a). It is not immediately obvious why the absorption increases. One explanation could be an increased film thickness. In AFM, however, we do not observe any clear increase in film thickness (SI, Figure S6). Another explanation could be the outgassing of volatile organic compounds from the film, which might originate from decomposition products of the organic ligands. The relative decrease in the organic content of the film could give rise to absorption changes. In this case, however, one would expect a decrease in film thickness and a strong reduction in IR absorption of organic functional groups. As shown in an upcoming section, this is not the case. A change in the refractive index of the material, due to changes in the electronic environment or different packing of the crystals, is also a possibility, which would change the reflectance and absorption. From Figure 4b, we also observe a change in reflectance as a function of dose, with a similar but opposite trend to the absorption, as it decreases from 0.12 ± 0.02 to 0.07 ± 0.01. A change in refractive index is therefore a reasonable hypothesis. To determine what change in refractive index could induce changes in absorption and reflection like those observed, we perform simple optical modeling of our system based on a transfer matrix calculation model by the McGehee group,[37,38] in turn based on the work of Pettersson et al. and Peumans et al.[39,40] The results can be found in Figure S7 of the Supporting Information. We focus our analysis on a single wavelength (the excitation wavelength λ = 405 nm), as we expect the changes to be qualitatively similar for the full spectrum. We find that a reduction in the refractive index n from 1.9 to around 1.75 may result in similar changes as observed in our measurements and is therefore the likely origin of the observed changes in optical properties. These changes could result from the cross-linking and therefore rearrangement of the ligands (see below) although understanding the exact origin of the change in refractive index itself would require further investigation, which is challenging due to the small area of exposure.

Figure 4c shows a typical integrated PL intensity map of one of the exposed samples. The intensity is normalized to the 95th percentile intensity value as some pixels were extremely bright. The mean values and spread of the PL in all of the exposure fields can be found in Figure 4d. We observe a similar but opposite trend to the absorption: an initial fast decrease up to an exposure dose of 2000 μC cm^{-2}, from 0.70 ± 0.13 to 0.40 ± 0.07, followed by a plateau and eventually further decrease. The exposure does therefore alter the emission intensity. Most of this change seems to occur up to 2000 μC cm^{-2}, which coincides with the dose that yields well-defined features. Higher doses did not change the resolved features significantly, but it does seem to have a further effect on the PL properties.

From the relative changes in absorbance, +26.1%, and PL, −42.9%, one might estimate that the PLQY does decrease quite significantly by a factor of 2. This does, however, assume that the outcoupling is not changed in the exposed areas as the light is collected in an objective above the sample and the emission is not collected in every direction. A change in film roughness might, however, scatter more light into more shallow angles and the potential change in refractive index discussed above might also alter the outcoupling efficiency.

We measure radiative lifetime to understand the changes we measured in PL intensity. We measure unexposed as well as patterned $CsPbBr_3$ films via time-correlated single photon counting (TCSPC) with a pulsed 485 nm excitation laser. We fit the decay curves with a two-exponential model (eq 1), where the first term is a stretched exponential term to take into account the nature of nanocrystals.[22,41] As they are an assembly of very small, single, isolated crystals, there is likely a distribution of radiative decay rates as these rates can slightly vary from crystal to crystal, more so than in a three-dimensional (3D) bulk material. The stretch factor β is an indicator of how wide the distribution of rates is and can take a positive value below or equal to 1. A β of 1 indicates the limit

https://doi.org/10.1021/acsaem.1c03091
ACS Appl. Energy Mater. XXXX, XXX, XXX−XXX

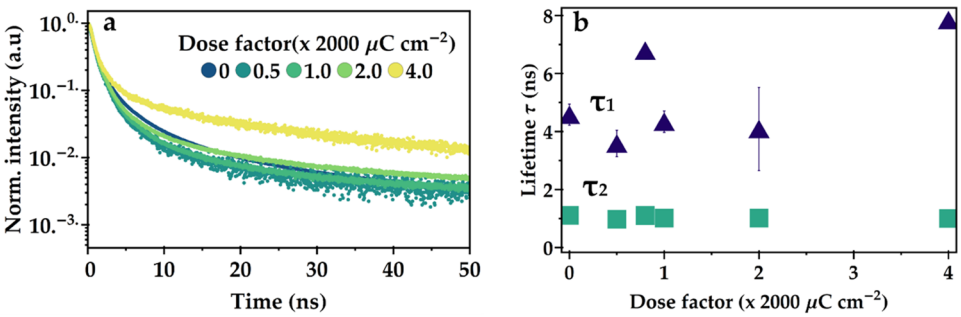

Figure 5. (a) Time-resolved photoluminescence of exposed $CsPbBr_3$. (b) Fitted lifetime components.

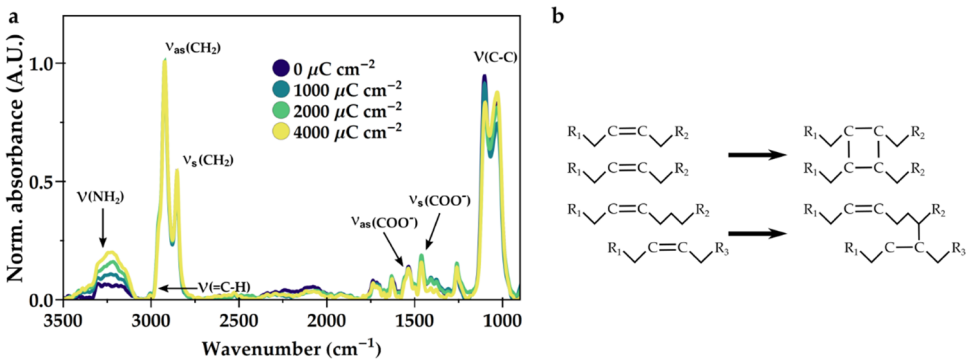

Figure 6. (a) FTIR spectra of e-beam-exposed $CsPbBr_3$. The films were exposed to different doses of 50 kV electrons. The spectra are normalized to the peak at 2950 cm^{-1}. The main changes are observed in the amine groups and the arrangement of the C−C bonds within the long ligand chains. (b) We propose that the double bonds that are present in both oleic acid and oleylamine can be attacked by radical species upon electron-beam exposure and can cross-link to form new C−C bonds between chains, thereby creating a network of interconnected ligands.

where only one rate is present, and we can ignore the stretched exponent

$$I(t) = A_1\, e^{(-t/\tau_1)^{\beta}} + A_2\, e^{-t/\tau_2} + b.g \quad (1)$$

. where $I(t)$ is the number of PL counts at time t, A_n is a dimensionless prefactor for each exponential term, τ_n is the characteristic lifetime, β is a dimensionless stretched exponential factor, and b.g. accounts for the background counts. The PL decay curves can be found in Figure 5. We find two lifetime components, one around 1 ns and one around 4 ns. The fast decay component is constant over different doses, while the longer component shows more spread. The observed spread is, however, also present from measuring different spots on the same sample. Fitted lifetime components of similar, unexposed samples can be found in appendix Figure S8. The stretched exponential β is stable around 0.75 (appendix Figure S9), which indicates a relatively small distribution of rates. Previously, we assigned the slower component to be the radiative lifetime, while the faster component is related to nonradiative processes. From these data points, however, it is not obvious that there is an increase in the nonradiative processes as the shorter lifetime component does not show a clear trend. It seems that the slower component increases with higher exposure doses, over 4000 $\mu C\ cm^{-2}$. This could be an indication that more trapping and detrapping are involved during the emission, causing more delayed fluorescence.[42]

The optical measurements therefore show an overall reduction in PL intensity with increasing exposure dose, although there is still relatively bright luminescence in developed structures with an unchanged line shape. In a similar trend, we observe an increase in absorption, likely due to changes in the refractive index caused by changes in the electronic environment of the crystals. The measured radiative lifetime does not change dramatically with dose, however. Although there are many processes that could influence the measured lifetime, it is possible that the fitted lifetime component is not purely radiative or nonradiative and therefore changes in nonradiative processes are less easily observed or that part of the changes in the measured PLQY result from differences in outcoupling, as speculated above.

To shed more light on the underlying patterning mechanism, we investigate the changes in the organic part of the perovskite by measuring Fourier transform infrared spectroscopy (FTIR). The spectra of differently exposed perovskite films can be found in Figure 6a. The changes are only small, indicating no major loss of organic material. This observation excludes outgassing of volatile organic compounds as a mechanism for changing absorption. The bands around 2950 and 2850 cm^{-1} correspond to asymmetric and symmetric CH_2 stretches, respectively. These are the most prominent bands due to the long carbon chains present in both oleic acid and oleylamine. The features around 1450 and 1550 cm^{-1} can be attributed to the COO^- anchoring group of oleic acid. These peaks are mostly unaffected by the exposure, indicating a good connection with the inorganic cations in the crystal cores, most likely Cs. An obvious change is the increase in the features between 3100 and 3300 cm^{-1}, which can be ascribed to several NH_2 modes. This change shows that with higher doses, more free amine groups are present in the film. These must originate from the amine binding group, which shows that some oleylamine ligands have detached. This ligand loss could be an explanation for the decrease in PLQY and may have an influence on the long-term stability of the perovskite, as not all facets of the perovskite will be properly passivated.

https://doi.org/10.1021/acsaem.1c03091
ACS Appl. Energy Mater. XXXX, XXX, XXX−XXX

We also observe a change in the wavenumber range around 1000−1100 cm^{-1}. These peaks are related to stretches between two carbon atoms in a chain. The ratio between the high-wavenumber peak and the low-wavenumber peak is continuously shifting toward the latter with increasing dose. This points to the creation of new C−C bonds. Overall, we hypothesize that the long ligands, oleylamine and oleic acid, partly cross-link upon exposure, as observed before.[22] Figure 6b shows possible cross-linking pathways. The high energy of the incoming electrons can create free electrons with a broad range of energies. Due to subsequent elastic and inelastic scattering, excited states within the molecule, as well as reactive holes, ionizations, and radicals, are generated.[43] As the energy of bonds like C−C and C−H are on the order of 3.6 and 4.4 eV, it is possible to break these bonds. Finally, it is possible to capture slower electrons in antibonding orbitals, which will lead to dissociation of bonds and reactive radicals as well.[44] These reactive species can attack double bonds and promote the formation of new bonds.[45] The increase in the feature between 1000 and 1100 cm^{-1} shows that new C−C bonds are being created, presumably by cross-linking at the double-bond position. The low concentration of the double-bond feature makes it, however, difficult to properly quantify. In combination with partial ligand detachment, which leads to charged surfaces, the nanocrystals are likely to form larger clusters of interconnected nanocrystals. This clustering strongly reduces the solubility of the crystals, thereby creating an insoluble material. The oleates are not affected, thereby keeping luminescence mostly intact. In e-beam lithography, the high-energy electrons will mostly pass through the patterning material entirely, as can be deduced from Monte Carlo simulations of electron (SI, Figure S10), even with thicker films. Since the patterning mechanism is induced by ligand changes, we believe that the ligands will have a bigger influence on the patterning sensitivity than the core crystals and therefore other perovskite compounds will likely behave in a similar way to $CsPbBr_3$. To increase sensitivity, however, other ligand chemistries may be favorable.

OUTLOOK AND CONCLUSIONS

We have patterned $CsPbBr_3$ nanocrystals in a simple one-step e-beam lithography process into structures down to 100s of nanometer with doses of around 2000 $\mu C\ cm^{-2}$. The patterns are well resolved down to about 100 nm and show excellent contrast. We observe a reduction in the relative PLQY of the material after processing, but luminescence remains bright and the radiative decay time scale is relatively stable. We attribute the patterning mechanism to cross-linking of the surface ligands. The ligands, next to passivating the surface and providing colloidal stability, thus also function as the scaffold that insolubilizes the perovskite nanocrystal clusters to form a pattern. The amine ligands, however, partially detach from the crystal, thereby reducing the passivation.

The required dose for patterning is relatively high, and further optimizing the cross-linking chemistry would be valuable for large-scale implementation, especially because this patterning technique is compatible with EUVL. EUV is rapidly becoming the new standard for high-volume lithography. Optimizing the cross-linking by increasing the number of double bonds and using strong anchoring groups should enhance the sensitivity and simultaneously increase stability.

The e-beam patterning of perovskite nanocrystals at the nanoscale presented here can be useful to pursue better-performing devices, for instance, by making use of nanophotonic structures to engineer the emissive properties.

EXPERIMENTAL METHODS

Chemicals. Hexane (anhydrous) and toluene (anhydrous) were purchased from VWR. Lead bromide ($PbBr_2$, 98% pure) was purchased from TCI. Cesium carbonate (Cs_2CO_3, 99.5% pure), 1-octadecene (ODE, technical grade 90%), oleic acid (OA, technical grade 90%), oleylamine (OlAm, technical grade 90%), tetrahydrofuran (THF, anhydrous, >99.9% pure), acetone (ACE, analytical grade), isopropanol (IPA, analytical grade), and methanol (MeOH, analytical grade) were purchased from Sigma-Aldrich. Double-side polished silicon wafers were purchased from Siegert Wafer. ITO-coated glass microscopic slides (19 mm × 19 mm) were purchased from Diamond Coatings.

Nanocrystal Synthesis. Synthesis of the $CsPbBr_3$ nanocrystals was performed via a recipe adapted from Lu et al.[34] and Protesescu et al.[5] First, cesium oleate precursor was prepared by adding 1.63 g of Cs_2CO_3 with 15.8 mL of OA with 34.2 mL of ODE into a three-neck flask in a glovebox to ensure oxygen- and water-free conditions. The flask was attached to a Schlenk line and evacuated 3× and under a flow of N_2; then, the solution was heated to 110 °C under continuous stirring for 3 h until all precursors were dissolved and a clear solution with the color of melted butter had formed. The solution was cooled to room temperature, and small amounts were taken from this stock solution.

For the final nanocrystal synthesis, 0.138 g $PbBr_2$ was combined in a glovebox with 0.5 mL OlAm, 0.5 mL OA, and 10 mL ODE in a 50 mL three-neck flask. The flask was evacuated 3× and refilled with N_2. Subsequently, the flask was heated to 120 °C and left for 1 h to degas and boil off any water. The precursor dissolved, and a clear, cream-colored solution formed. Subsequently, the temperature was increased to 150 °C and 1 mL of Cs-oleate precursor solution was injected. After a couple of seconds, the solution turned bright yellow/green and the reaction was subsequently quenched in an ice bath. The reaction solution showed bright green fluorescence under UV.

To purify the reaction product, 1 mL of the reaction liquid was mixed with 1 mL of toluene, followed by centrifugation at 12 000 rpm for 10 min. The supernatant was discarded, and the precipitate was dispersed in 200 μL of hexane. The solution was centrifuged for 10 min at 12 000 rpm again, and the supernatant was again discarded. Finally, the precipitate was dispersed in 100 μL toluene and centrifuged 5 min at 4000 rpm. The supernatant was kept as the final solution. This process was repeated until all of the reaction solution was purified.

Film Preparation. Samples for exposure were made by spin-coating thin films of nanocrystals on clean silicon substrates. The substrates were cleaned by subsequent sonication in soap water, distilled (DI) water, ACE, and IPA and finally 15 min of oxygen plasma. Nanocrystal solutions were filtered (0.2 μm poly(tetrafluoroethylene) (PTFE) filter) and spin-coated at 2500 rpm for 20 s, resulting in films with a thickness of around 100 nm.

High-Energy e-Beam Exposure. E-beam exposure was done in a Raith Voyager commercial e-beam lithography system with a voltage of 50 kV, an LC30 column mode with a 0.135 nA beam current. Films were developed in a (1:1 vol) mixture of THF and chloroform immediately after exposure.

Scanning Electron Microscope. SEM images were taken by an FEI Verios 460 at voltages between 5 and 10 kV at 100 pA.

Atomic Force Microscopy. AFM images were taken on a Veeco Dimension 3100 (Bruker) in tapping mode. Linescan frequency was 1 Hz.

Photoluminescence. Photoluminescence of samples was measured using a WITec alpha300 SR confocal microscope with a 100× Zeiss objective (NA 0.9). A 405 nm Thorlabs S1FC405 fiber-coupled laser diode was used as an excitation source. A 405 nm notch filter was used to remove the laser light in the detection path, which was coupled to the detector. Light is collected in reflection on a UHTC 300 VIS WITec spectrometer. The PL spectra were converted to the

https://doi.org/10.1021/acsaem.1c03091
ACS Appl. Energy Mater. XXXX, XXX, XXX−XXX

energy scale using a Jacobian transformation.[46] The setup can be used to record single spectra as well as perform spatial PL mapping.

Photoluminescence Lifetime Measurements. Fluorescence lifetimes were recorded with a homebuilt TCSPC setup (PicoQuant PDL 828 "Sepia II" and a PicoQuant HydraHarp 400 multichannel) in an inverted microscope with an Olympus 60x Plan Apochromat water immersion objective. The samples were excited by a 485 nm laser (PicoQuant LDH-D-C-485), which was pulsed at a repetition rate of 10 MHz. The excitation laser signal was blocked from the detection path by a Thorlabs FEL-500 long-pass filter in combination with a 488-NF notch filter.

Absorption Measurements. Absorption measurements were performed in a custom-built integrating sphere setup, described in previous work.[36] Absorbance was measured at 405 nm by recording the transmission, scattering, and reflection of a 405 nm Thorlabs S1FC405 fiber-coupled laser diode.

Optical Microscope. Optical microscopic images were recorded with a Zeiss, AxioCam ICc 5 equipped with a 20×/0.2 objective.

■ ASSOCIATED CONTENT

Supporting Information

The Supporting Information is available free of charge at https://pubs.acs.org/doi/10.1021/acsaem.1c03091.

> Extra SEM images of EUV and e-beam exposed nanocrystal films, raw PL data, optical microscopic images, full absorption and reflectance maps of exposed nanocrystal films, extra AFM height map, transfer matrix optical modeling of the perovskite film, extra TCSPC data, and Monte Carlo simulations of electron trajectories in CASINO (PDF)

■ AUTHOR INFORMATION

Corresponding Author

Bruno Ehrler − *Center for Nanophotonics, AMOLF, 1098 XG Amsterdam, The Netherlands;* orcid.org/0000-0002-5307-3241; Email: ehrler@amolf.nl

Authors

Christian D. Dieleman − *Center for Nanophotonics, AMOLF, 1098 XG Amsterdam, The Netherlands; Advanced Research Center for Nanolithography, 1098 XG Amsterdam, The Netherlands;* orcid.org/0000-0002-6571-7657

Julia van der Burgt − *Center for Nanophotonics, AMOLF, 1098 XG Amsterdam, The Netherlands*

Neha Thakur − *Advanced Research Center for Nanolithography, 1098 XG Amsterdam, The Netherlands;* orcid.org/0000-0001-5252-0938

Erik C. Garnett − *Center for Nanophotonics, AMOLF, 1098 XG Amsterdam, The Netherlands;* orcid.org/0000-0002-9158-8326

Complete contact information is available at: https://pubs.acs.org/10.1021/acsaem.1c03091

Funding

The research leading to these results has received funding from the European Community's Seventh Framework Programme (FP7/2007−2013) under grant agreement no. 312284 (CALIPSO). This work has been carried out at AMOLF and ARCNL. ARCNL is a public−private partnership of UvA, VU, NWO, and ASML. This work is part of the research program Mat4Sus, which is financed by The Netherlands Organisation for Scientific Research (NWO).

Notes

The authors declare no competing financial interest.

■ ACKNOWLEDGMENTS

The authors would like to thank Bob Drent, Dimitry Lamers, and Igor Hoogsteder for technical support with e-beam exposure and SEM imaging and Dr. Biplap Patra for input on nanocrystal synthesis.

■ REFERENCES

(1) Murray, C. B.; Norris, D. J.; Bawendi, M. G. Synthesis and Characterization of Nearly Monodisperse CdE (E = Sulfur, Selenium, Tellurium) Semiconductor Nanocrystallites. *J. Am. Chem. Soc.* **1993**, *115*, 8706−8715.

(2) Moreels, I.; Justo, Y.; De Geyter, B.; Haustraete, K.; Martins, J. C.; Hens, Z. Size-Tunable, Bright, and Stable PbS Quantum Dots: A Surface Chemistry Study. *ACS Nano* **2011**, *5*, 2004−2012.

(3) Bailey, R. E.; Nie, S. Alloyed Semiconductor Quantum Dots: Tuning the Optical Properties without Changing the Particle Size. *J. Am. Chem. Soc.* **2003**, *125*, 7100−7106.

(4) Lim, S. J.; Zahid, M. U.; Le, P.; Ma, L.; Entenberg, D.; Harney, A. S.; Condeelis, J.; Smith, A. M. Brightness-Equalized Quantum Dots. *Nat. Commun.* **2015**, *6*, No. 8210.

(5) Protesescu, L.; Yakunin, S.; Bodnarchuk, M. I.; Krieg, F.; Caputo, R.; Hendon, C. H.; Yang, R. X.; Walsh, A.; Kovalenko, M. V. Nanocrystals of Cesium Lead Halide Perovskites (CsPbX3, X = Cl, Br, and I): Novel Optoelectronic Materials Showing Bright Emission with Wide Color Gamut. *Nano Lett.* **2015**, *15*, 3692−3696.

(6) Akkerman, Q. A.; D'Innocenzo, V.; Accornero, S.; Scarpellini, A.; Petrozza, A.; Prato, M.; Manna, L. Tuning the Optical Properties of Cesium Lead Halide Perovskite Nanocrystals by Anion Exchange Reactions. *J. Am. Chem. Soc.* **2015**, *137*, 10276−10281.

(7) Vybornyi, O.; Yakunin, S.; Kovalenko, M. V. Polar-Solvent-Free Colloidal Synthesis of Highly Luminescent Alkylammonium Lead Halide Perovskite Nanocrystals. *Nanoscale* **2016**, *8*, 6278−6283.

(8) Protesescu, L.; Yakunin, S.; Kumar, S.; Bär, J.; Bertolotti, F.; Masciocchi, N.; Guagliardi, A.; Grotevent, M.; Shorubalko, I.; Bodnarchuk, M. I.; Shih, C. J.; Kovalenko, M. V. Dismantling the "Red Wall" of Colloidal Perovskites: Highly Luminescent Formamidinium and Formamidinium-Cesium Lead Iodide Nanocrystals. *ACS Nano* **2017**, *11*, 3119−3134.

(9) Wang, A.; Guo, Y.; Muhammad, F.; Deng, Z. Controlled Synthesis of Lead-Free Cesium Tin Halide Perovskite Cubic Nanocages with High Stability. *Chem. Mater.* **2017**, *29*, 6493−6501.

(10) Akkerman, Q. A.; Gandini, M.; Di Stasio, F.; Rastogi, P.; Palazon, F.; Bertoni, G.; Ball, J. M.; Prato, M.; Petrozza, A.; Manna, L. Strongly Emissive Perovskite Nanocrystal Inks for High-Voltage Solar Cells. *Nat. Energy* **2017**, *2*, No. 16194.

(11) Zhou, D.; Liu, D.; Pan, G.; Chen, X.; Li, D.; Xu, W.; Bai, X.; Song, H. Cerium and Ytterbium Codoped Halide Perovskite Quantum Dots: A Novel and Efficient Downconverter for Improving the Performance of Silicon Solar Cells. *Adv. Mater.* **2017**, *29*, No. 1704149.

(12) Zhang, J.; Wang, Q.; Zhang, X.; Jiang, J.; Gao, Z.; Jin, Z.; Liu, S. High-Performance Transparent Ultraviolet Photodetectors Based on Inorganic Perovskite CsPbCl3 Nanocrystals. *RSC Adv.* **2017**, *7*, 36722−36727.

(13) Gong, M.; Sakidja, R.; Goul, R.; Ewing, D.; Casper, M.; Stramel, A.; Elliot, A.; Wu, J. Z. High-Performance All-Inorganic CsPbCl3 Perovskite Nanocrystal Photodetectors with Superior Stability. *ACS Nano* **2019**, *13*, 1772−1783.

(14) Chen, Q.; Wu, J.; Ou, X.; Huang, B.; Almutlaq, J.; Zhumekenov, A. A.; Guan, X.; Han, S.; Liang, L.; Yi, Z.; Li, J.; Xie, X.; Wang, Y.; Li, Y.; Fan, D.; Teh, D. B. L.; All, A. H.; Mohammed, O. F.; Bakr, O. M.; Wu, T.; Bettinelli, M.; Yang, H.; Huang, W.; Liu, X. All-Inorganic Perovskite Nanocrystal Scintillators. *Nature* **2018**, *561*, 88−93.

(15) Heo, J. H.; Shin, D. H.; Park, J. K.; Kim, D. H.; Lee, S. J.; Im, S. H. High-Performance Next-Generation Perovskite Nanocrystal Scintillator for Nondestructive X-Ray Imaging. *Adv. Mater.* **2018**, *30*, No. 1801743.

(16) Li, G.; Rivarola, F. W. R.; Davis, N. J. L. K.; Bai, S.; Jellicoe, T. C.; de la Peña, F.; Hou, S.; Ducati, C.; Gao, F.; Friend, R. H.; Greenham, N. C.; Tan, Z.-K. Highly Efficient Perovskite Nanocrystal Light-Emitting Diodes Enabled by a Universal Crosslinking Method. *Adv. Mater.* **2016**, *28*, 3528−3534.
(17) Hu, H.; Wu, L.; Tan, Y.; Zhong, Q.; Chen, M.; Qiu, Y.; Yang, D.; Sun, B.; Zhang, Q.; Yin, Y. Interfacial Synthesis of Highly Stable CsPbX3/Oxide Janus Nanoparticles. *J. Am. Chem. Soc.* **2018**, *140*, 406−412.
(18) Liu, H.; Tan, Y.; Cao, M.; Hu, H.; Wu, L.; Yu, X.; Wang, L.; Sun, B.; Zhang, Q. Fabricating CsPbX3-Based Type i and Type II Heterostructures by Tuning the Halide Composition of Janus CsPbX3/ZrO2 Nanocrystals. *ACS Nano* **2019**, *13*, 5366−5374.
(19) Mao, J.; Sha, W. E. I.; Zhang, H.; Ren, X.; Zhuang, J.; Roy, V. A. L.; Wong, K. S.; Choy, W. C. H. Novel Direct Nanopatterning Approach to Fabricate Periodically Nanostructured Perovskite for Optoelectronic Applications. *Adv. Funct. Mater.* **2017**, *27*, No. 1606525.
(20) Vila-Liarte, D.; Feil, M. W.; Manzi, A.; Garcia-Pomar, J. L.; Huang, H.; Döblinger, M.; Liz-Marzán, L. M.; Feldmann, J.; Polavarapu, L.; Mihi, A. Templated-Assembly of CsPbBr3 Perovskite Nanocrystals into 2D Photonic Supercrystals with Amplified Spontaneous Emission. *Angew. Chem., Int. Ed.* **2020**, *59*, 17750−17756.
(21) Prins, F.; Kim, D. K.; Cui, J.; De Leo, E.; Spiegel, L. L.; McPeak, K. M.; Norris, D. J. Direct Patterning of Colloidal Quantum-Dot Thin Films for Enhanced and Spectrally Selective Out-Coupling of Emission. *Nano Lett.* **2017**, *17*, 1319−1325.
(22) Dieleman, C. D.; Ding, W.; Wu, L.; Thakur, N.; Bespalov, I.; Daiber, B.; Ekinci, Y.; Castellanos, S.; Ehrler, B. Universal Direct Patterning of Colloidal Quantum Dots by (Extreme) Ultraviolet and Electron Beam Lithography. *Nanoscale* **2020**, *12*, 11306−11316.
(23) Xin, B.; Pak, Y.; Mitra, S.; Almalawi, D.; Alwadai, N.; Zhang, Y.; Roqan, I. S. Self-Patterned CsPbBr 3 Nanocrystals for High-Performance Optoelectronics. *ACS Appl. Mater. Interfaces* **2019**, *11*, 5223−5231.
(24) Mehetor, S. K.; Ghosh, H.; Pradhan, N. Blue-Emitting CsPbBr3 Perovskite Quantum Rods and Their Wide-Area 2D Self-Assembly. *ACS Energy Lett.* **2019**, *4*, 1437−1442.
(25) Huang, X.; Guo, Q.; Kang, S.; Ouyang, T.; Chen, Q.; Liu, X.; Xia, Z.; Yang, Z.; Zhang, Q.; Qiu, J.; Dong, G. Three-Dimensional Laser-Assisted Patterning of Blue-Emissive Metal Halide Perovskite Nanocrystals inside a Glass with Switchable Photoluminescence. *ACS Nano* **2020**, *14*, 3150−3158.
(26) Zhan, W.; Meng, L.; Shao, C.; Wu, X.; Shi, K.; Zhong, H. In Situ Patterning Perovskite Quantum Dots by Direct Laser Writing Fabrication. *ACS Photonics* **2021**, *8*, 765−770.
(27) Altintas, Y.; Torun, I.; Yazici, A. F.; Beskazak, E.; Erdem, T.; Serdar Onses, M.; Mutlugun, E. Multiplexed Patterning of Cesium Lead Halide Perovskite Nanocrystals by Additive Jet Printing for Efficient White Light Generation. *Chem. Eng. J.* **2020**, *380*, No. 122493.
(28) Zou, C.; Chang, C.; Sun, D.; Böhringer, K. F.; Lin, L. Y. Photolithographic Patterning of Perovskite Thin Films for Multicolor Display Applications. *Nano Lett.* **2020**, *20*, 3710−3717.
(29) Xing, D.; Lin, C. C.; Ho, Y. L.; Kamal, A. S. A.; Wang, I. T.; Chen, C. C.; Wen, C. Y.; Chen, C. W.; Delaunay, J. J. Self-Healing Lithographic Patterning of Perovskite Nanocrystals for Large-Area Single-Mode Laser Array. *Adv. Funct. Mater.* **2021**, *31*, No. 2006283.
(30) Palazon, F.; Akkerman, Q. A.; Prato, M.; Manna, L. X-Ray Lithography on Perovskite Nanocrystals Films: From Patterning with Anion-Exchange Reactions to Enhanced Stability in Air and Water. *ACS Nano* **2016**, *10*, 1224−1230.
(31) Meng, L.; You, J.; Yang, Y. Addressing the Stability Issue of Perovskite Solar Cells for Commercial Applications. *Nat. Commun.* **2018**, No. 5265.
(32) Ran, J.; Dyck, O.; Wang, X.; Yang, B.; Geohegan, D. B.; Xiao, K. Electron-Beam-Related Studies of Halide Perovskites: Challenges and Opportunities. *Adv. Energy Mater.* **2020**, *10*, No. 1903191.
(33) Kovalenko, M. V.; Protesescu, L.; Bodnarchuk, M. I. Properties and Potential Optoelectronic Applications of Lead Halide Perovskite Nanocrystals. *Science* **2017**, 745−750.
(34) Lu, C.; Wright, M. W.; Ma, X.; Li, H.; Itanze, D. S.; Carter, J. A.; Hewitt, C. A.; Donati, G. L.; Carroll, D. L.; Lundin, P. M.; Geyer, S. M. Cesium Oleate Precursor Preparation for Lead Halide Perovskite Nanocrystal Synthesis: The Influence of Excess Oleic Acid on Achieving Solubility, Conversion, and Reproducibility. *Chem. Mater.* **2019**, *31*, 62−67.
(35) Stelmakh, A.; Aebli, M.; Baumketner, A.; Kovalenko, M. V. On the Mechanism of Alkylammonium Ligands Binding to the Surface of CsPbBr3 Nanocrystals. *Chem. Mater.* **2021**, 5962−5973.
(36) Mann, S. A.; Sciacca, B.; Zhang, Y.; Wang, J.; Kontoleta, E.; Liu, H.; Garnett, E. C. Integrating Sphere Microscopy for Direct Absorption Measurements of Single Nanostructures. *ACS Nano* **2017**, *11*, 1412−1418.
(37) Burkhard, G. F.; Hoke, E. T.; McGehee, M. D. Accounting for Interference, Scattering, and Electrode Absorption to Make Accurate Internal Quantum Efficiency Measurements in Organic and Other Thin Solar Cells. *Adv. Mater.* **2010**, *22*, 3293−3297.
(38) Burkhard, G. F.; Hoke, E. T. Transfer Matrix Optical Modeling. https://web.stanford.edu/group/mcgehee/transfermatrix/TransferMatrix.pdf (accessed Sept 03, 2021).
(39) Pettersson, L. A. A.; Roman, L. S.; Inganäs, O. Modeling Photocurrent Action Spectra of Photovoltaic Devices Based on Organic Thin Films. *J. Appl. Phys.* **1999**, *86*, 487.
(40) Peumans, P.; Yakimov, A.; Forrest, S. R. Small Molecular Weight Organic Thin-Film Photodetectors and Solar Cells. *J. Appl. Phys* **2003**, *93*, 3693.
(41) Schöps, O.; Le Thomas, N.; Woggon, U.; Artemyev, M. V. Recombination Dynamics of CdTe/CdS Core-Shell Nanocrystals. *J. Phys. Chem. B* **2006**, *110*, 2074−2079.
(42) Vonk, S. J. W.; Fridriksson, M. B.; Hinterding, S. O. M.; Mangnus, M. J. J.; van Swieten, T. P.; Grozema, F. C.; Rabouw, F. T.; van der Stam, W. Trapping and Detrapping in Colloidal Perovskite Nanoplatelets: Elucidation and Prevention of Nonradiative Processes through Chemical. *J. Phys. Chem. C* **2020**, *124*, 8047.
(43) Kozawa, T.; Tagawa, S. Radiation Chemistry in Chemically Amplified Resists. *Jpn. J. Appl. Phys.* **2010**, *49*, No. 030001.
(44) Narasimhan, A.; Wisehart, L.; Grzeskowiak, S.; Ocola, L. E.; Denbeaux, G.; Brainard, R. L. What We Don't Know About EUV Exposure Mechanisms. *J. Photopolym. Sci. Technol.* **2017**, *30*, 113−120.
(45) Mattson, E. C.; Cabrera, Y.; Rupich, S. M.; Wang, Y.; Oyekan, K. A.; Mustard, T. J.; Halls, M. D.; Bechtel, H. A.; Martin, M. C.; Chabal, Y. J. Chemical Modification Mechanisms in Hybrid Hafnium Oxo-Methacrylate Nanocluster Photoresists for Extreme Ultraviolet Patterning. *Chem. Mater.* **2018**, *30*, 6192−6206.
(46) Mooney, J.; Kambhampati, P. Get the Basics Right: Jacobian Conversion of Wavelength and Energy Scales for Quantitative Analysis of Emission Spectra. *J. Phys. Chem. Lett.* **2013**, *4*, 3316−3318.

https://doi.org/10.1021/acsaem.1c03091
ACS Appl. Energy Mater. XXXX, XXX, XXX−XXX